Safe Motion Planning for Steerable Needles Using Cost Maps Automatically Extracted from Pulmonary Images

Mengyu Fu, Alan Kuntz, Robert J. Webster III, and Ron Alterovitz

Abstract— Lung cancer is the deadliest form of cancer, and early diagnosis is critical to favorable survival rates. Definitive diagnosis of lung cancer typically requires needle biopsy. Common lung nodule biopsy approaches either carry significant risk or are incapable of accessing large regions of the lung, such as in the periphery. Deploying a steerable needle from a bronchoscope and steering through the lung allows for safe biopsy while improving the accessibility of lung nodules in the lung periphery. In this work, we present a method for extracting a cost map automatically from pulmonary CT images, and utilizing the cost map to efficiently plan safe motions for a steerable needle through the lung. The cost map encodes obstacles that should be avoided, such as the lung pleura, bronchial tubes, and large blood vessels, and additionally formulates a cost for the rest of the lung which corresponds to an approximate likelihood that a blood vessel exists at each location in the anatomy. We then present a motion planning approach that utilizes the cost map to generate paths that minimize accumulated cost while safely reaching a goal location in the lung.

I. INTRODUCTION

Lung cancer is the deadliest form of cancer in the United States [1], and early diagnosis is critical to survival. While medical imaging is used to identify potentially cancerous nodules in the lung, definitive diagnosis typically requires biopsy [2]. Transthoracic biopsy, in which a needle is inserted through the chest wall to the nodule, is a commonly used biopsy technique. However, it carries a significant risk of pneumothorax (lung collapse), a serious complication [3], and errors in needle targeting can mitigate the procedure's effectiveness [4]. An alternative approach is transoral biopsy in which a bronchoscope is inserted into the airway to biopsy the nodule. The transoral approach significantly lowers the risk of pneumothorax, but many nodules, especially those in the peripheral lung (near the chest wall) or far from larger bronchial tubes, are inaccessible using current devices. To combine the benefits of the transthoracic and transoral biopsy approaches without the drawbacks, we are developing a robotic system that deploys a steerable needle from a bronchoscope [5], [6] to enable accurate access to nodules throughout the lung for biopsy.

In this paper, we present an approach for automatically extracting relevant anatomical information from pulmonary medical images and planning a safe motion for a steerable needle to a desired target in the lung. The steerable needle

M. Fu, A. Kuntz, and R. Alterovitz are with the Department of Computer Science, University of North Carolina at Chapel Hill, Chapel Hill, NC 27599, USA. {mfu,adkuntz,ron}@cs.unc.edu

R. J. Webster III is with the Department of Mechanical Engineering, Vanderbilt University, Nashville, TN 37235, USA.
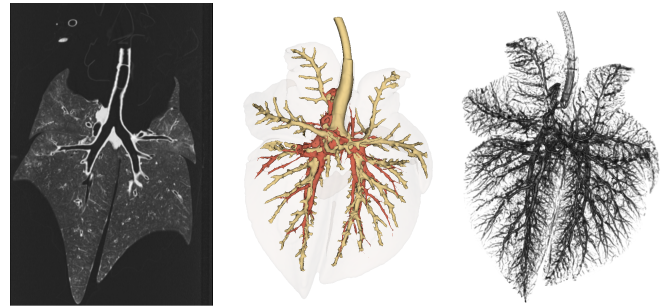
Fig. 1. To facilitate the safe guidance of a steerable needle to a target within a lung for biopsy, we extract anatomical information from a pre-procedure pulmonary CT image. Left: One slice of the example volumetric porcine pulmonary CT image. Middle: Automatically segmented obstacles, namely the boundary of lung (cream), the bronchial tree (gold), and large blood vessels (red). Right: Automatically extracted vasculature, in which darker voxels have higher cost due to the increased risks associated with damaging or puncturing these structures during a biopsy. The pulmonary cost map encodes costs for obstacles and small blood vessels.
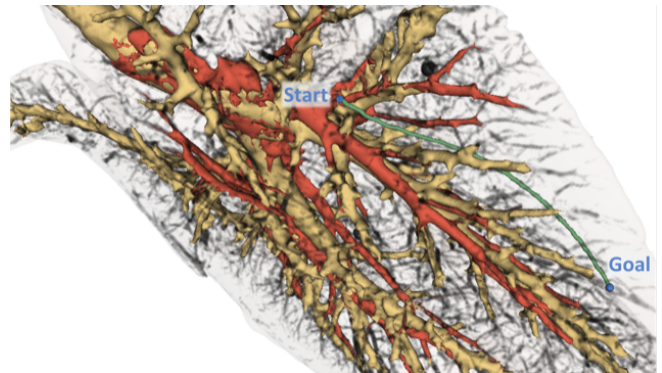

Fig. 2. An example planned path (green) for the steerable needle in a porcine lung. The path starts from an initial pose (start) and reaches a target point (goal) while avoiding obstacles and minimizing the cost along the path.

is deployed from the bronchoscope, exits the bronchial tube, and steers through the lung parenchyma (the tissue outside the bronchial tubes) to the target. The lung parenchyma is cluttered with obstacles that the steerable needle should avoid. These obstacles include large blood vessels (which could result in clinically significant hemorrhage if damaged), the bronchial tubes (which could damage the needle once the needle has entered the parenchyma), and the lung pleura (the outer membrane of the lung, which could lead to lung collapse if pierced). The lung parenchyma also includes many small blood vessels, and it is impossible in most cases to guide a needle to a target in a manner that avoids all blood vessels. In addition to avoiding the obstacles specified above, a safe needle plan should also minimize the piercing

of small blood vessels when possible to further reduce the risk of bleeding.

We first present an approach for automatically extracting information from preoperative medical Computed Tomography (CT) images and representing the information in a form that is usable by a motion planner for steerable needles. We use a cost map to encode the risk of steering the needle through specific locations in the lung. To enable avoidance of obstacles in the lung (i.e., the large blood vessels, the bronchial tubes, and the boundary of the lung), we automatically extract their locations from the CT image and encode them in the cost map as infinite cost. To minimize damage to small blood vessels, we encode a cost for them based on a cylindrical shape model designed to identify vasculature. We illustrate the automatically computed obstacles and vasculature in Fig. 1.

We next present a steerable needle motion planner that uses the cost map to compute motion plans that avoid obstacles while minimizing damage to vasculature. We assume the needle is steered during breath holds in which the inflation of the lung matches the preoperative CT image. To generate motion plans we use a sampling-based motion planner that is based on the Rapidly-Exploring Random Tree (RRT) algorithm [7]. Our motion planner builds on a previously-developed motion planner for steerable needles [8], extending it to consider a pulmonary cost map. The motion planner uses the cost map to ensure a plan avoids obstacles and to compute the cost of a plan based on the needle trajectory's accumulated cost in the cost map (see Fig. 2). We also speed up the motion planner's obstacle collision detection by leveraging geometric simplifications of the needle with respect to the obstacles in the cost map. The motion planning process repeats as time allows, allowing us to generate plans with lower cost in an anytime manner.

We demonstrate the accuracy of our automatic methods for computing the vasculature in the lung by comparing our results with images hand segmented by experts from the VESSEL12 challenge [9]. We then automatically generate a cost map from a CT scan of an ex vivo porcine lung, and we demonstrate that our motion planner, using the cost map, results in safer steerable needle motion plans in the lung.

II. RELATED WORK

A. Lung Segmentation

Prior work on motion planning for steerable needles in the lung considered obstacles that were manually segmented and only included larger bronchial tubes and blood vessels [8], [6]. In this work, we compute a pulmonary cost map by automatically segmenting the lung boundary, bronchial tubes, and large and small blood vessels from a CT image.

For a comprehensive survey of segmentation methods for pulmonary structures we direct the reader to [10]. Different lung boundary segmentation methods have been proposed, including region growing, optimal thresholding, and graph-cut [11]. For airway segmentation, single thresholding, rule-based methods, fuzzy logic, fuzzy connectedness, wavefront propagation, and mathematical morphology have all been

used [12], [13]. There are also many methods for vessel segmentation which rely on a combination of vascular models, image features, and extraction schemes [14]. These methods can be broadly classified into the following categories: Hessian-based vesselness filters [15], region growing methods, thresholding-based methods, fuzzy connectedness methods, and machine learning based methods [10]. In some cases, a Hessian-based filter is applied to the image to obtain a response known as "vesselness". In our method, we adapt the region growing approach for lung boundary segmentation [11], the morphology-based approach for airway segmentation [12], and the Hessian-based vesselness enhancement approach for vascular segmentation [15].

B. Steerable Needle Motion Planning

After generating the pulmonary cost map, we plan the motion of a steerable needle to a clinical target. We specifically focus on steerable needles that are flexible and have an asymmetric tip (e.g., a bevel), which exerts an asymmetric force on soft tissue when inserted, causing the needle to curve in the direction of the bevel [16], [17], [18]. These needles can be rotated axially at their base to change the direction of curvature during insertion, and the turning radius of the needle during insertion can be controlled via duty cycling [19]. To represent the kinematics of steerable needles, we use a 3D unicycle model [17], [20], [16], [18].

Motion planning and control algorithms have been developed to guide steerable needles to targets [21], [18]. A variety of motion planning approaches have been proposed, including optimization-based approaches [22], [23], fractal tree-based planning [24], and sampling-based motion planning [25]. Motion planners have explicitly considered the impact of motion uncertainty and tissue deformations. Approaches have included computing motion plans that maximize the probability of reaching a target while avoiding obstacles [26], [27], considering error propagation [28], adapting helical trajectories [29], fast trajectory correction [30], closed-loop control using feedback from medical imaging [31], and using a sliding mode controller that does not require a priori knowledge of the needle's turning radius [32]. High-frequency replanning has successfully been used as a way to combine motion planning and control [33], [34]. This paper builds on the approach of Patil et al. [25], which uses a variant of a rapidly-exploring random tree [35] and specifically considers the geometry of the needle's kinematics to efficiently generate motion plans.

Motion planners can use a cost map to evaluate plan quality. Caborni et al. developed a cost function that accounts for path length, clearance from no-go areas, and accumulated risk along a 2D path for a steerable flexible probe in the brain [36]. Cost maps in 2D have been used when planning motions for autonomous vehicles (e.g., [37], [38], [39]). King et al. demonstrate efficient computation of a non-round object's footprint in 2D cost maps [40]. We approximate the steerable needle's motion in the cost map by building on the approach in [39] to efficiently and conservatively account for the shape of the needle in the cost map.

III. PROBLEM DEFINITION

Our method consists of two phases. The first is to automatically generate a pulmonary cost map from a volumetric CT image of the lung. The second is to plan safe motions for the steerable needle based on the pulmonary cost map.

A. Computing a Pulmonary Cost Map from a CT Image

Let I be the pulmonary volumetric CT image of size $i_{max} \times j_{max} \times k_{max}$ voxels, and $\mathbf{x} = (i, j, k)$ be an ordered tuple of indices where $i = 0, \ldots, i_{max}-1; j = 0, \ldots, j_{max}-1; k = 0, \ldots, k_{max} - 1$. We denote the intensity of voxel $\mathbf{x}$ in I as $I(\mathbf{x})$ in Hounsfield Units (HU) with a typical range of $[-1000, 3000]$. The size of a single voxel in I is $S_{voxel} = [s_1, s_2, s_3]$. Note that $i_{max}, j_{max}, k_{max}, s_1, s_2$, and s_3 depend on the settings and model of the CT scanner.

Our first objective is to compute a pulmonary cost map M_{cost} of the same size as I that encodes the costs associated with traversing each corresponding voxel of I with a needle. We define $M_{cost}(\mathbf{x}) \in [0, 1] \cup \{\infty\}$ as the cost of traversing voxel $\mathbf{x}$ in I. If the voxel $\mathbf{x}$ in I is part of an obstacle (i.e., a bronchial tube, the space outside the lung surface, or a large blood vessel with an approximate radius greater than a physician-specified parameter r_{vessel}), then we assign $M_{cost}(\mathbf{x}) = \infty$. Otherwise, we assign $M_{cost}(\mathbf{x}) = \alpha \in [0, 1]$ which corresponds to vesselness response, an approximate likelihood that the voxel contains a vessel. A higher value indicates higher risk when steering a needle through that voxel.

B. Steerable Needle Motion Planning in a Cost Map

A configuration $\mathbf{q} \in \mathcal{SE}(3)$ of the steerable needle is defined by the pose of the needle's tip, which we represent as a 4×4 matrix

$$\mathbf{q} = \left(\begin{array}{cc} \mathbf{R} & \mathbf{p} \\ \mathbf{0} & 1 \end{array} \right),$$

where $\mathbf{R} \in \mathcal{SO}(3)$ is the rotation matrix defining the orientation of the needle tip and $\mathbf{p} \in \mathbb{R}^3$ denotes the position of the needle tip in the coordinate frame of the real world.

We control the steerable needle by inserting and axially rotating the needle about its base. So we define the control input as $\mathbf{u} = \{d, \phi, \kappa\}$, where $d \in \mathbb{R}$ is insertion distance, $\phi \in [0, 2\pi)$ is the axial rotation angle of the tip which defines the direction in which the needle curves, and $\kappa \in \mathbb{R}^+ \cup \{0\}$ is the curvature value achieved using duty cycling [19]. The curvature value ranges from 0 to κ_{max} where κ_{max} is an experimentally derived parameter dictated by the mechanical properties of the needle and the tissue in which it is being inserted.

Let $\Pi = \{\mathbf{q}_0, \mathbf{q}_1, \ldots, \mathbf{q}_{n-1}\}$ be a motion plan specified by a sequence of n configurations representing a continuous path in the needle's configuration space. A motion plan is collision-free if the steerable needle does not intersect any voxel $\mathbf{x}$ for which $M_{cost}(\mathbf{x}) = \infty$. More formally, we denote the set of intersected voxels in a single step as

$$V_i = \text{VoxelsIntersected}(\mathbf{q}_i, \mathbf{q}_{i+1}).$$

The set of all voxels intersected along a path is $V_\Pi = \cup_{i=0}^{n-2} V_i$. A motion plan Π is collision-free when $M_{cost}(\mathbf{v}) < \infty$ for all $\mathbf{v} \in V_\Pi$. We define the cost of a motion plan Π as

$$\text{Cost}(\Pi) = \sum_{\mathbf{v} \in V_\Pi} M_{cost}(\mathbf{v}). \tag{1}$$

Our objective is to find a collision-free motion plan for the steerable needle from a starting configuration $\mathbf{q}_{start}$ to a goal configuration $\mathbf{q}_{goal}$ which minimizes cost. We note that $\mathbf{p}_{goal}$ is specified while $\mathbf{R}_{goal}$ is not, because as long as the needle tip reaches the goal position, the biopsy is a success, so there is no need to specify the goal orientation. We represent the steerable needle's kinematics (including the constraint of maximum curvature on the path) using the general inequality $\mathbf{g}(\Pi) \geq 0$. Finally, the motion planning problem can be formulated as:

$$\Pi^* = \underset{\Pi}{\text{argmin}} \, \text{Cost}(\Pi)$$
$$\text{Subject to :}$$
$$M_{cost}(\mathbf{v}) < \infty \text{ for all } \mathbf{v} \in V_\Pi$$
$$\mathbf{g}(\Pi) \geq 0 \tag{2}$$
$$\mathbf{q}_0 = \mathbf{q}_{start}$$
$$\mathbf{p}_{n-1} = \mathbf{p}_{goal}$$

where Π^* is an optimal motion plan.

IV. METHOD

Our method first generates the pulmonary cost map based on the CT image. Then, given a starting needle pose and goal position in the lung, the motion planner computes motions for the steerable needle that connect the starting pose with the goal position while avoiding all obstacles, minimizing damage to the patient, and enforcing maximum curvature constraints associated with the needle's kinematics. As time allows, the motion planner computes more paths, and the path is selected that minimizes the path's accumulated cost in M_{cost} while satisfying constraints according to (2).

A. Computing the Pulmonary Cost Map from a CT Image

Fig. 3 shows the overall pipeline for extracting the pulmonary cost map M_{cost}. To construct M_{cost}, our method first sets the cost for voxels inside obstacles to infinite cost, and then sets the rest of the voxels to a cost representing their vesselness response. We discuss below how we segment the various structures of the lung and incorporate them into the pulmonary cost map.

1) Lung Boundary: We segment the lung boundary using a seeded 3D region growing method. This method grows a region from a user-selected seed point inside the lung parenchyma (for in vivo lungs) or inside the background region (for ex vivo lungs) until the lung boundary is encountered. This approach is effective in segmenting the lung boundary since there is a significant voxel intensity difference between the lung parenchyma and the surrounding regions (e.g., tissues outside an in vivo lung or the tray and air outside an ex vivo lung). Since region growing may exclude certain structures within the lung due to their higher
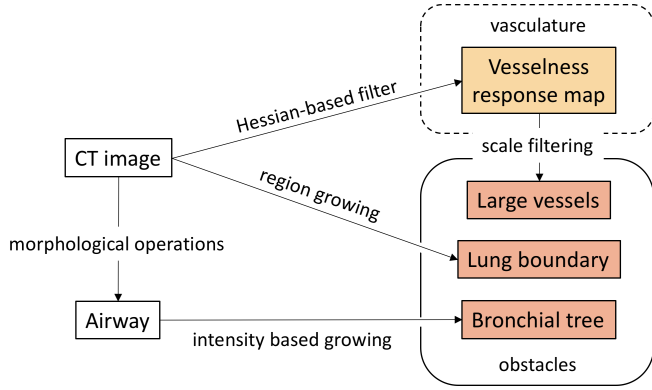
Fig. 3. The pipeline for segmenting the anatomy to create the pulmonary cost map M_{cost}. We assign voxels inside obstacles a cost of ∞. Vasculature is categorized into large and small blood vessels, with large vessels treated as obstacles and the remaining vessels assigned costs between 0 and 1.

voxel intensities (e.g., major blood vessels and bronchial tubes), we apply a morphological closing procedure to fill these cavities, which yields a segmentation of the volume of the lungs. We treat each voxel $\mathbf{x}$ external to the lungs as an obstacle by setting $M_{\mathrm{cost}}(\mathbf{x}) = \infty$.

2) Bronchial Tree: To segment the bronchial tree, we begin by leveraging the fact that bronchial tubes contain air, so the interior of the bronchial tubes have low intensity voxels in the CT image. We use a local minima map which indicates, for each voxel, how much lower its intensity is compared to the maximum intensity in its neighboring area of a certain size. We construct local minima maps at multiple scales, enabling us to extract the airway of bronchial tubes of different sizes. Finally, we grow the airway structure to incorporate the tissue that composes the bronchial tube walls.

More specifically, we compute the local minima maps based on ideas from [12]. We perform grayscale morphological operations in a slice-by-slice manner. Usually in CT images, voxel size is structured such that $s_3 > s_1 = s_2$, so slices are extracted along the z-axis to get square pixels. First, we apply a 4-connected neighborhood averaging to suppress noise. Then for a 2D image slice I_s, we perform the following grayscale reconstructing operations to compute a local minima map slice L_s:

$$J_0^n = I_s \bullet B_n = (I_s \oplus B_n) \ominus B_n, \quad n = 1, 2, \ldots, N,$$
$$J_{k+1}^n = \max\left(J_k^n \ominus B_1, I_s\right), \quad k = 0, 1, \ldots, k_{\max}$$
$$D^n = J_{k_{\max}}^n - I_s,$$
$$L_s = \max_n\left(D^n\right),$$

where $\bullet$, $\oplus$, and $\ominus$ are grayscale morphological closing, erosion and dilation respectively; $\max()$ computes a pixel-by-pixel maximum; $-$ computes a pixel-by-pixel difference; J_k^n is an intermediate image in the kth iteration when doing grayscale reconstruction on scale n; B_1 is a 4-connected binary structuring element (SE), and $B_n = nB_1 = B_1 \oplus B_1 \cdots \oplus B_1$ $(n-1$ dilations$)$; N is the number of SEs applied, where the maximum reconstruction scale we use is $N = 12$; $J_{k_{\max}}^n$ is an image obtained and $k_{\max}$ is the total number of iterations when J_k^n has reached idempotency; and D^n is
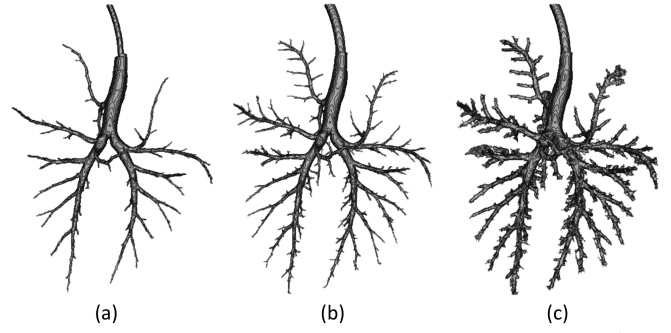

Fig. 4. Results of bronchial tree segmentation. (a) Major airway A; (b) refined airway A_{post}; (c) reconstructed airway wall W.

the difference map of scale n, containing bright clusters of pixels that mark the location and depth of the local minima in slice I_s. We then obtain a 3D local minima map, denoted as L, by stacking the 2D L_s back together.

From a seed point in the trachea, we then perform adaptive region growing in L to segment the major airway region A (see Fig. 4(a)). To refine the segmentation, we then use the following post-processing step

$$I_{\mathrm{tmp}}(\mathbf{x}) = \begin{cases} I(\mathbf{x}), & \mathbf{x} \notin A \\ r, & \mathbf{x} \in A \end{cases}$$
$$L_{\mathrm{post}} = I_{\mathrm{tmp}} \bullet B_1 - I,$$

where r is a replacing intensity, which is 0 in our experiments. We then apply adaptive region growing in L_{post} to obtain a refined segmentation of the airway, denoted as A_{post} (see Fig. 4(b)). This, however, results in a segmentation of the *internal* volume of the bronchial tree. Because the bronchial tube walls can be non-trivially thick, we must then reconstruct the airway wall region W. We do this by growing outward from A_{post}. W first includes all neighboring voxels of A_{post}. Then, in a layer-by-layer manner, we include voxels whose absolute intensity is above some threshold $T_{\mathrm{abs}} = -600$ and for which the maximum intensity difference from neighboring voxels that are already included in W is below another threshold $T_{\mathrm{dif}} = 10$. Fig. 4(c) shows the reconstructed airway wall W. In the cost map, for each voxel $\mathbf{x} \in W \cup A_{\mathrm{post}}$ we set $M_{\mathrm{cost}}(\mathbf{x}) = \infty$.

3) Vasculature: In the CT image, we assume blood vessels present as cylindrical shapes, where the pixel intensities on the cross-section of the cylinder appear as a 2D Gaussian distribution. Our goal is to compute a "vesselness" response for each voxel of the image, where a higher vesselness response value corresponds to a higher likelihood that the voxel contains a vessel. We compute the vesselness response by applying Hessian-based filters to the image to discriminate vessel-like structures from other structures. We employ a multi-scale strategy to consider blood vessels with different radii and to identify the large blood vessels. For voxels contained in the large blood vessels, we set M_{cost} to infinity since large blood vessels are obstacles. For all remaining voxels inside the lung boundary, we set M_{cost} to the computed vesselness response to indicate the risk associated with traveling through the small blood vessels.

We compute vesselness response for voxels in the lung

using a combination of methods building upon the Hessian-based filter proposed by Frangi et al. [15]. The eigenvalues of the Hessian matrix at each voxel can be used to distinguish points inside and outside a curvilinear structure. Our vessel-ness response function uses these eigenvalues to determine the local likelihood of the presence of blood vessels at each voxel. To compute the Hessian matrix $H(\mathbf{x};\sigma)$, in which we need second derivatives of $I(\mathbf{x})$, we use the second derivatives of a Gaussian [15]. For example,

$$I_{xx}(\mathbf{x};\sigma) = \sigma^{2\gamma} I(\mathbf{x}) * \left\{ \frac{\partial^2}{\partial x^2} G(\mathbf{x};\sigma) \right\}, \qquad (3)$$

where $*$ denotes convolution, $G(\mathbf{x};\sigma)$ is the isotropic Gaussian function with standard deviation σ [mm], and parameter γ was introduced to define normalized derivatives in [41]. Here we set γ to 1 for scale invariance. The Gaussian allows us to both reduce noise and to tune the filter response to the specific radii of blood vessels, corresponding to the standard deviation of the Gaussian.

Let λ_1, λ_2 and λ_3 be the eigenvalues of $H(\mathbf{x};\sigma)$, where $|\lambda_1| \le |\lambda_2| \le |\lambda_3|$. As in [15], three measures are computed:

$$R_A = \frac{|\lambda_2|}{|\lambda_3|}, \quad R_B = \frac{|\lambda_1|}{\sqrt{|\lambda_2\lambda_3|}}, \quad S = \sqrt{\lambda_1^2 + \lambda_2^2 + \lambda_3^2}.$$

R_A and R_B account for the deviation from plate-like and blob-like structures respectively, and S is the Frobenius norm of the Hessian. Then the vesselness response is computed by

$$R(\mathbf{x};\sigma) = \begin{cases} 0, & \lambda_2 \ge 0 \text{ or } \lambda_3 \ge 0 \\ \left(1-\exp\left(\frac{-R_A^2}{2\alpha^2}\right)\right)\exp\left(\frac{-R_B^2}{2\beta^2}\right)\left(1-\exp\left(\frac{-S^2}{2c^2}\right)\right), & \text{else} \end{cases}$$

where the sensitivity control parameters are $\alpha = 0.5$, $\beta = 0.5$, and $c = 70$ in our experiments. As analyzed in [15], vesselness response is maximized when the vessel radius approximately matches σ. Thus, to compute vesselness response for blood vessels with different radii, we compute the vesselness response at multiple scales. The $\gamma-$normalization in (3) balances the response of different scales, ensuring responses of different scales have comparable ranges.

We also adapt the multi-region method in [42] to allow us to apply the above methods separately to different regions of the lung. Denote $\mathbf{S}$ as a set of σs for multi-scale vesselness response computation. When $\mathbf{S}$ contains a σ that is much larger than the radius of the vessels lying in the region, the vesselness response is too large at voxels corresponding to spaces between thin vessels that are close to each other. This may result in blurring of small vessels caused by excessive smoothing due to Gaussian filtering with a large σ. To address this issue, we apply large σs only to the center regions of the lung where the vessels are thicker. This allows us to more accurately represent small vasculature than if we apply the above methods uniformly.

Using the set of regions defined in [42], we compute the vesselness response in each region separately. We have

$$\mathbf{S} = \begin{cases} \{1\}, & 0 < r \le 1 \\ \{1, \sqrt{2}, 2\}, & 1 < r \le 2 \\ \{1, \sqrt{2}, 2, 2\sqrt{2}\}, & 2 < r \le 2\sqrt{2} \\ \{1, \sqrt{2}, 2, 2\sqrt{2}, 4\}, & 2\sqrt{2} < r \end{cases} \qquad (4)$$
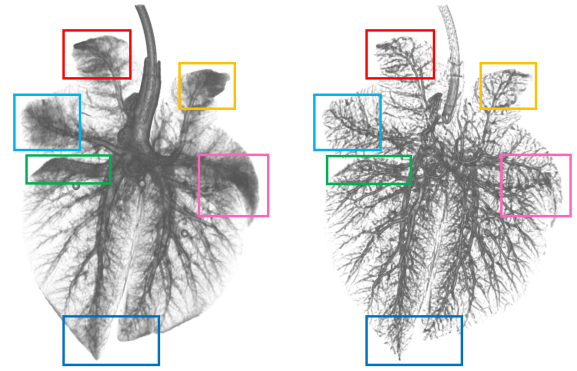

Fig. 5. For the pulmonary cost map, our method based on vesselness response (right) provides more detailed information about the vasculature relative to using only pixel intensities from the CT image (left), where we visualize higher intensities using darker voxels. We highlight corresponding regions using boxes of the same color.

where r is the distance in mm between a voxel and its nearest lung surface. We define the vesselness response as

$$R(\mathbf{x}) = \max_{\sigma \in \mathbf{S}} R(\mathbf{x};\sigma), \qquad (5)$$

then take the resulting vesselness responses from each region and apply the value directly in M_{cost}. A benefit of computing vesselness response based on second derivatives is that it can identify vessel structures well in regions of varying intensities (see Fig. 5) by relying more on relative intensity rather than absolute intensity.

Because there are large blood vessels in the lung that the needle must always avoid, we need to include vessels larger than a certain radius in the set of obstacles. With the previous vesselness response function, frequently a voxel will have a high response to multiple σs, making it difficult to identify large blood vessels. To address this, we apply a different Hessian-based filter modified from [42]. The vesselness response function for large vessels is then defined as

$$R_L(\mathbf{x};\sigma) = \begin{cases} 0, & \lambda_2 \ge 0 \text{ or } \lambda_3 \ge 0 \\ \frac{-\lambda_2}{I_{\text{ref}} - \max(I(\mathbf{x}), I_{\text{max}})}, & \text{else} \end{cases}$$

where we have $I_{\text{ref}} = 300$ and $I_{\text{max}} = 200$. Equations (4) and (5) are then applied as before using R_L. This multi-scale vesselness response computation allows us to identify the approximate radius of a vessel based on which σ corresponds to the maximum response produced by the voxels corresponding to the vessel. Let $\sigma(\mathbf{x})$ be the σ to which voxel $\mathbf{x}$ has maximum response. Thus according to a user defined r_{vessel} and response threshold R_T, we segment out voxels with $\sigma(\mathbf{x}) \ge r_{\text{vessel}}$ and $R(\mathbf{x}) \ge R_T$ as candidate regions of large blood vessels. In this work, we use $r_{\text{vessel}} = 2\sqrt{2}$ [mm] and $R_T = 400$. We then denoise the results by removing candidate regions with volume less than 1000 voxels. We assign an infinite cost in M_{cost} for the remaining candidate regions. See Fig. 1 for an example of M_{cost}.

B. Motion Planning for the Steerable Needle in the Lung

After constructing the pulmonary cost map, we are ready to plan motions for the steerable needle in the lung. Given a starting needle pose and a goal position, we compute many
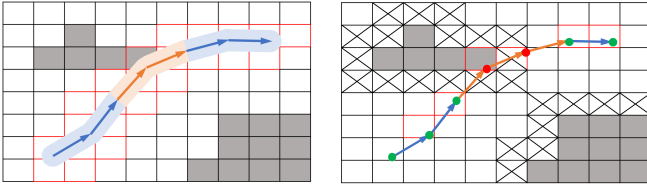
Fig. 6. A comparison of the accurate collision detection and the faster approximate collision detection strategy in 2D. For both figures, obstacles are shown in gray, voxels that need to be checked have red boundaries, collision-free steps are shown in blue, and in-collision steps in orange. Left: Accurate collision detection, wherein many voxels are checked during collision detection. Right: Approximate collision detection, where only voxels that the end points fall into are checked. Voxels resulting from the inflation are shown crossed, collision-free ending points are shown in green, otherwise in red.

motion plans iteratively as time allows. At each iteration, we generate a single motion plan for the needle that connects the starting pose with the goal point and ensures no part of the path collides with an obstacle. We then compute the cost of the path based on M_{cost}. If the cost is less than that of any path we have found previously, we keep it as the best path. This continues in an anytime fashion, allowing our method to find better and better paths as computation time allows.

The motion planner that runs at each iteration of the method requires as input (1) M_{cost}, (2) the needle's radius r_{needle}, (3) the needle's maximum achievable curvature $\kappa_{\max}$, (4) voxel size S_{voxel}, and (5) a starting pose $\mathbf{q}_{\text{start}} \in \mathcal{SE}(3)$ and a goal site $\mathbf{p}_{\text{goal}} \in \mathbb{R}^3$.

We utilize an adaptation of the motion planner presented in [8]. The planner incrementally builds a tree of robot states that are reachable from $\mathbf{q}_{\text{start}}$ by collision-free paths. During the tree construction, the planner samples a point in $\mathbb{R}^3$, and selects the nearest state $\mathbf{q}_{\text{near}}$ in the tree to the sampled point. It then computes a control $\mathbf{u}$ which when applied to $\mathbf{q}_{\text{near}}$ steers the needle toward the sampled point up to a distance defined by the step size t, resulting in a state $\mathbf{q}_{\text{new}}$. If edge $(\mathbf{q}_{\text{near}}, \mathbf{q}_{\text{new}})$ is collision-free, then $\mathbf{q}_{\text{new}}$ is added to the tree. This proceeds until the goal position is reached or the allotted computation time is exceeded.

We further adapt the motion planner in [8] to achieve fast collision detection with respect to the obstacles. To do so, the pulmonary cost map is modified by taking the needle's radius and a safety margin into consideration. Recall that the needle tip radius is r_{needle} and denote a user defined safety margin as r_{safe}. If we finely discretize the path the needle takes through the lung, the footprint of a single step can be approximated as a capsule (the volume described by linearly sweeping a sphere) parameterized by step size t and radius $r_{\text{total}} = r_{\text{needle}} + r_{\text{safe}}$. To perform completely accurate collision detection, we would check every voxel that the capsule intersects to see if it is an obstacle (see Fig. 6), requiring a large amount of computation. To achieve faster collision detection, we conservatively approximate this operation by inflating the obstacles by $a_i = \left\lceil \frac{r_{\text{total}}}{s_i} \right\rceil$, $i = 1, 2, 3$. The resulting a_1, a_2, a_3 describe the size of an ellipsoid measured in number of voxels. The inflating operation can then be performed by morphological dilation on a binary obstacle map defined by the infinite cost voxels in

M_{cost}. Morphological dilation is an approximation of the Minkowski sum which can be quickly computed on sets of voxels. The voxels corresponding to the inflated obstacles are then assigned infinite cost in M_{cost}. After the obstacles in M_{cost} are so inflated, we then treat the needle tip as a point robot, checking only the voxels at which a step ends (see Fig. 6). This allows the collision checking to be done by a simple array lookup. As a trade-off, the motion planner must then be constrained by the maximum step size. We compute the maximum step size by

$$d_{\max} = \min_{i=x,y,z} (a_i s_i)$$

$$t_{\max} = 2\sqrt{(d_{\max})^2 - r_{\text{total}}^2}$$

where $d_{\max}$ is the allowed maximum distance from the center of a sampled point to points inside the footprint. That is to say, as long as the step size is smaller than $t_{\max}$, this approximate collision detection provides a conservative substitute to the accurate collision detection.

V. RESULTS

We first evaluate our constructed cost map M_{cost} using example CT images of in vivo human lungs from the VESSEL12 challenge [9]. In this data set, involving three CT scans, there are a total of 882 manually segmented points, among which 281 points are identified as belonging to vasculature. We evaluate our automatically generated cost map's ability to correctly identify both true positives and true negatives with respect to the manually segmented points. We use the F_1 score, defined as $F_1 = (2 \times \text{Precision} \times \text{Recall})/(\text{Precision} + \text{Recall})$, to evaluate the results. Our method achieves a maximum F_1 score of 0.9709 averaged across the three scans, validating our cost map.

We evaluate the motion planner in a simulated lung scenario, using a cost map automatically extracted from the CT image of an ex vivo porcine lung. We generate three scenarios of varying difficulty which consist of a staring pose $\mathbf{q}_{\text{start}}$ and a goal position that is within the theoretical reachable workspace of the needle defined by its maximum curvature value. In our experiments $\kappa_{\max}$ is set as $(0.121\text{m})^{-1}$, a value experimentally derived in prior work [43]. We compare the following methods:

(1) Steerable Needle RRT with Cost Map: This is the motion planning method proposed in this paper, which builds an RRT with only collision-free states and selects paths based on the optimization formulation in (2).

(2) Steerable Needle RRT: Consistent with prior needle steering work, in this variant we avoid obstacles (using M_{cost} only for collision detection) and select the path with the shortest length.

(3) Voxel Intensity RRT: In this variant we use the original medical image as a cost map, ensuring that all intensity values are positive by adding $-\min(I(\mathbf{x}))$ to the intensity of all the voxels.

We compare the performance of the different methods from two perspectives: the ability of the method to find a collision-free path quickly, and the quality of the resulting

paths. For each scenario we ran the methods 10 times with different random seeds and allow the methods to execute for 500 seconds per run. We then average the results over the 10 runs. The final path cost for a path was computed using (1). A run is considered successful if the method returned a collision-free path before the time limit. The results are shown in Fig. 7.

The results show that our method, Steerable Needle RRT with Cost Map, is not only capable of finding collision-free paths quickly, but also shows an advantage over other methods in resulting path cost, both in the short and long term. Also note that the behavior of our method in a single run is such that the path cost decreases monotonically, resulting in better and better plans over time. The increase in the average cost value for our method shown early in Scenario 3 is due to the averaging of path costs over multiple runs in which the first valid path returns later in some runs. When comparing against Steerable Needle RRT without the cost map, our method in most cases results in path costs that are 50% lower, indicating that many fewer small vessels are punctured. Our method also performs well when compared against the Voxel Intensity RRT, generating successful paths more quickly in the medium and hard difficulty scenarios, and with improved average cost across all scenarios. This improvement shows that computing the cost map using our image processing method yields better motion planning results compared to only using pixel intensities of the raw CT image.

VI. Conclusion

We presented a method for extracting a cost map automatically from pulmonary CT images, and utilize the map to efficiently plan safe motions for a steerable needle through the lung. The cost map encodes obstacles that must be avoided, including the lung boundary, bronchial tubes, and large blood vessels. The cost map additionally formulates a cost for the rest of the lung which corresponds to an approximate likelihood that a blood vessel exists at each location in the anatomy. We then presented an efficient motion planning approach that uses the cost map to generate paths that minimize accumulated cost while safely reaching a goal location in the lung. The method performs in an anytime fashion, improving the quality of the motion plan as computation time allows.

In future work, we plan to extend our approach to enable automatic motion planning for not only the steerable needle but also additional phases of the lung biopsy robot's deployment, including bronchoscope deployment and control over the needle's angle of entry into the parenchyma [8]. We also plan to explicitly consider lung motion and evaluate our methods with experiments in ex vivo porcine lung tissue.

Acknowledgement

References

[1] American Cancer Society, "Cancer Facts & Figures," American Cancer Society, Tech. Rep., 2018.

[2] G. Krishna and M. K. Gould, "Minimally invasive techniques for the diagnosis of peripheral pulmonary nodules," *Current Opinion in Pulmonary Medicine*, vol. 14, pp. 282–286, 2008.

[3] R. S. Wiener, L. M. Schwartz, S. Woloshin, and H. G. Welch, "Population-based risk for complications after transthoracic needle lung biopsy of a pulmonary nodule: an analysis of discharge records," *Annals of Internal Medicine*, vol. 155, no. 3, pp. 137–144, 2011.

[4] N. Kothary, L. Lock, D. Y. Sze, and L. V. Hofmann, "Computed tomography–guided percutaneous needle biopsy of pulmonary nodules: Impact of nodule size on diagnostic accuracy," *Clinical Lung Cancer*, vol. 10, no. 5, pp. 360–363, 2009.

[5] P. J. Swaney, A. W. Mahoney, A. A. Remirez, E. Lamers, B. I. Hartley, R. H. Feins, R. Alterovitz, and R. J. Webster III, "Tendons, concentric tubes, and a bevel tip: three steerable robots in one transoral lung access system," in *IEEE Int. Conf. Robotics and Automation (ICRA)*, May 2015, pp. 5378–5383.

[6] A. Kuntz, P. J. Swaney, A. Mahoney, R. H. Feins, Y. Z. Lee, R. J. Webster III, and R. Alterovitz, "Toward transoral peripheral lung access: Steering bronchoscope-deployed needles through porcine lung tissue," in *Hamlyn Symposium on Medical Robotics*, Jun 2016, pp. 9–10.

[7] S. M. LaValle and J. J. Kuffner, "Rapidly-exploring random trees: Progress and prospects," in *Algorithmic and Computational Robotics: New Directions*, B. R. Donald and Others, Eds. Natick, MA: AK Peters, 2001, pp. 293–308.

[8] A. Kuntz, L. G. Torres, R. H. Feins, R. J. Webster III, and R. Alterovitz, "Motion planning for a three-stage multilumen transoral lung access system," in *Proc. IEEE/RSJ Int. Conf. Intelligent Robots and Systems (IROS)*, Sept. 2015, pp. 3255–3261.

[9] Consortium for Open Medical Image Computing, "VESsel SEgmentation in the Lung 2012," vessel12.grand-challenge.org, accessed: 2018-02.

[10] E. M. Van Rikxoort and B. Van Ginneken, "Automated segmentation of pulmonary structures in thoracic computed tomography scans: a review," *Physics in Medicine & Biology*, vol. 58, no. 17, pp. R187–R220, 2013.

[11] S. Hu, E. A. Hoffman, and J. M. Reinhardt, "Automatic lung segmentation for accurate quantitation of volumetric x-ray CT images," *IEEE Trans. Medical Imaging*, vol. 20, no. 6, pp. 490–498, 2001.

[12] D. Aykac, E. A. Hoffman, G. McLennan, and J. M. Reinhardt, "Segmentation and analysis of the human airway tree from three-dimensional x-ray CT images," *IEEE Trans. Medical Imaging*, vol. 22, no. 8, pp. 940–950, 2003.

[13] P. Lo, B. Van Ginneken, J. M. Reinhardt, T. Yavarna, P. A. De Jong, B. Irving, C. Fetita, M. Ortner, R. Pinho, and J. Sijbers, "Extraction of airways from CT (EXACT'09)," *IEEE Trans. Medical Imaging*, vol. 31, no. 11, pp. 2093–2107, 2012.

[14] R. D. Rudyanto, S. Kerkstra, E. M. Van Rikxoort, C. Fetita, P.-Y. Brillet, C. Lefevre, W. Xue, X. Zhu, J. Liang, I. Öksüz, *et al.*, "Comparing algorithms for automated vessel segmentation in computed tomography scans of the lung: the vessel12 study," *Medical Image Analysis*, vol. 18, no. 7, pp. 1217–1232, 2014.

[15] A. F. Frangi, W. J. Niessen, K. L. Vincken, and M. A. Viergever, "Multiscale vessel enhancement filtering," in *Int. Conf. Medical Image Computing and Computer-Assisted Intervention (MICCAI)*. Springer, 1998, pp. 130–137.

[16] R. J. Webster III, A. M. Okamura, N. J. Cowan, G. S. Chirikjian, K. Goldberg, and R. Alterovitz, "Distal bevel-tip needle control device and algorithm," United States Patent 7,822,458, May 2005.

[17] R. J. Webster III, J. S. Kim, N. J. Cowan, G. S. Chirikjian, and A. M. Okamura, "Nonholonomic modeling of needle steering," *Int. J. Robotics Research*, vol. 25, no. 5-6, pp. 509–525, May 2006.

[18] N. J. Cowan, K. Goldberg, G. S. Chirikjian, G. Fichtinger, R. Alterovitz, K. B. Reed, V. Kallem, W. Park, S. Misra, and A. M. Okamura, "Robotic needle steering: design, modeling, planning, and image guidance," in *Surgical Robotics: System Applications and Visions*, J. Rosen, B. Hannaford, and R. M. Satava, Eds. Springer, 2011, ch. 23, pp. 557–582.

[19] D. Minhas, J. A. Engh, M. M. Fenske, and C. Riviere, "Modeling of needle steering via duty-cycled spinning," in *Proc. Int. Conf. IEEE Engineering in Medicine and Biology Society (EMBS)*, Aug. 2007, pp. 2756–2759.
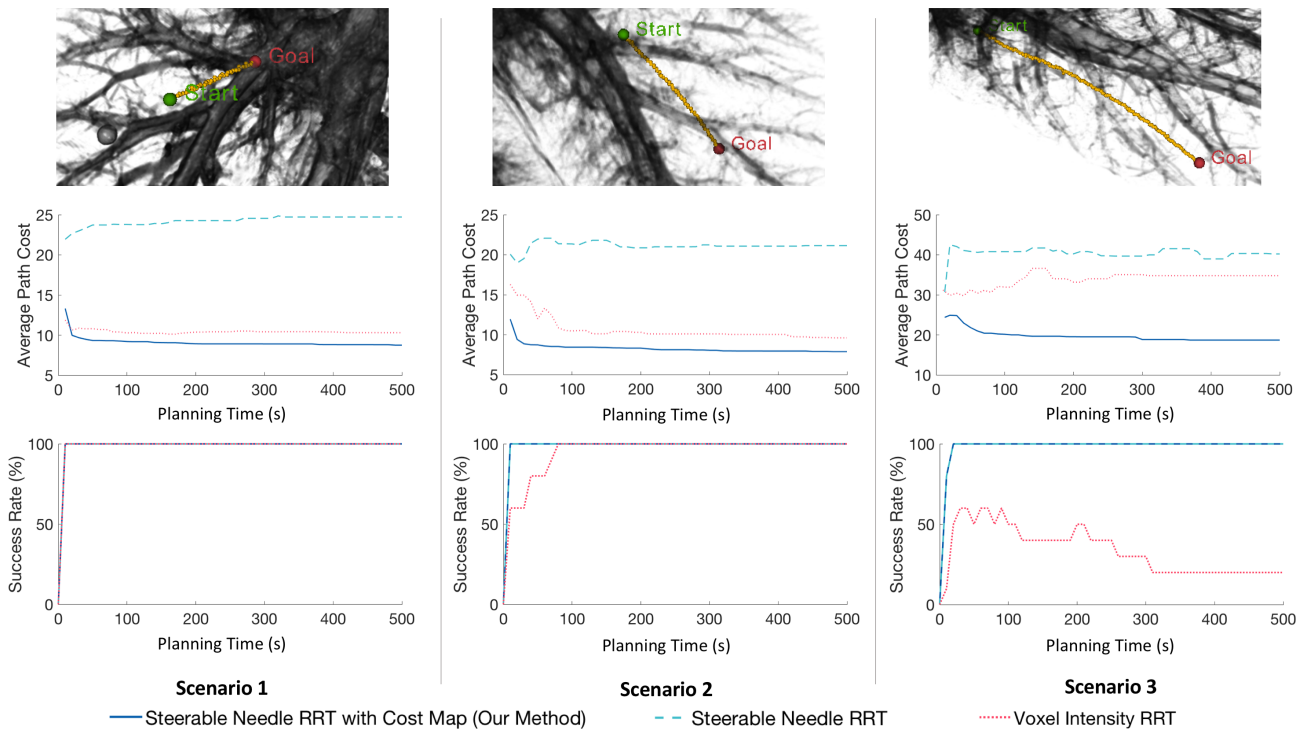
Fig. 7. Results of three methods in three scenarios of varying difficulty, with the least difficult on the left, medium difficulty in the middle, and the most difficult scenario on the right. In the top row we show the corresponding scenario in 3D, and visualize an example path (yellow) from the start point (green) to the goal point (red). In the middle row we show the average path cost over time of 10 runs, and the success rate over time in the bottom row.

[20] W. Park, J. S. Kim, Y. Zhou, N. J. Cowan, A. M. Okamura, and G. S. Chirikjian, "Diffusion-based motion planning for a nonholonomic flexible needle model," in *Proc. IEEE Int. Conf. Robotics and Automation (ICRA)*, Apr. 2005, pp. 4611–4616.

[21] K. B. Reed, A. Majewicz, V. Kallem, R. Alterovitz, K. Goldberg, N. J. Cowan, and A. M. Okamura, "Robot-assisted needle steering," *IEEE Robotics and Automation Magazine*, vol. 18, no. 4, pp. 35–46, 2011.

[22] R. Alterovitz, K. Goldberg, and A. M. Okamura, "Planning for steerable bevel-tip needle insertion through 2D soft tissue with obstacles," in *Proc. IEEE Int. Conf. Robotics and Automation (ICRA)*, Apr. 2005, pp. 1652–1657.

[23] V. Duindam, J. Xu, R. Alterovitz, S. Sastry, and K. Goldberg, "Three-dimensional motion planning algorithms for steerable needles using inverse kinematics," *Int. J. Robotics Research*, vol. 29, no. 7, pp. 789–800, June 2010.

[24] F. Liu, A. Garriga-Casanovas, R. Secoli, and F. Rodriguez y Baena, "Fast and adaptive fractal tree-based path planning for programmable bevel tip steerable needles," *IEEE Robotics and Automation Letters*, vol. 1, no. 2, pp. 601–608, 2016.

[25] S. Patil and R. Alterovitz, "Interactive motion planning for steerable needles in 3D environments with obstacles," in *Proc. IEEE Int. Conf. Biomedical Robotics and Biomechatronics (BioRob)*, Sept. 2010, pp. 893–899.

[26] R. Alterovitz, M. Branicky, and K. Goldberg, "Motion planning under uncertainty for image-guided medical needle steering," *Int. J. Robotics Research*, vol. 27, no. 11-12, pp. 1361–1374, Jan. 2008.

[27] S. Patil, J. van den Berg, and R. Alterovitz, "Motion planning under uncertainty in highly deformable environments," in *Robotics: Science and Systems (RSS)*, June 2011.

[28] W. Park, Y. Wang, and G. S. Chirikjian, "The path-of-probability algorithm for steering and feedback control of flexible needles," *Int. J. Robotics Research*, vol. 29, no. 7, pp. 813–830, June 2010.

[29] K. Hauser, R. Alterovitz, N. Chentanez, A. M. Okamura, and K. Goldberg, "Feedback control for steering needles through 3D deformable tissue using helical paths," in *Robotics: Science and Systems (RSS)*, June 2009.

[30] K. M. Seiler, S. P. Singh, S. Sukkarieh, and H. Durrant-Whyte, "Using Lie group symmetries for fast corrective motion planning," *Int. J. Robotics Research*, vol. 31, no. 2, pp. 151–166, Dec. 2011.

[31] M. C. Bernardes, B. V. Adorno, P. Poignet, and G. A. Borges, "Robot-assisted automatic insertion of steerable needles with closed-loop imaging feedback and intraoperative trajectory replanning," *Mechatronics*, vol. 23, pp. 630–645, July 2013.

[32] D. C. Rucker, J. Das, H. B. Gilbert, P. J. Swaney, M. I. Miga, N. Sarkar, and R. J. Webster III, "Sliding mode control of steerable needles," *IEEE Trans. Robotics*, vol. 29, no. 5, pp. 1289–1299, July 2013.

[33] S. Patil, J. Burgner, R. J. Webster III, and R. Alterovitz, "Needle steering in 3-D via rapid replanning," *IEEE Trans. Robotics*, vol. 30, no. 4, pp. 853–864, Aug. 2014.

[34] W. Sun, S. Patil, and R. Alterovitz, "High-frequency replanning under uncertainty using parallel sampling-based motion planning," *IEEE Trans. Robotics*, vol. 31, no. 1, pp. 104–116, Feb. 2015.

[35] S. M. LaValle, *Planning Algorithms*. Cambridge, U.K.: Cambridge University Press, 2006.

[36] C. Caborni, S. Y. Ko, E. De Momi, G. Ferrigno, and F. Rodriguez y Baena, "Risk-based path planning for a steerable flexible probe for neurosurgical intervention," in *Proc. IEEE Int. Conf. Biomedical Robotics and Biomechatronics (BioRob)*, 2012, pp. 866–871.

[37] Y. Kuwata, J. Teo, G. Fiore, S. Karaman, E. Frazzoli, and J. P. How, "Real-time motion planning with applications to autonomous urban driving," *IEEE Trans. Control Systems Technology*, vol. 17, no. 5, pp. 1105–1118, 2009.

[38] M. Pivtoraiko, R. A. Knepper, and A. Kelly, "Differentially constrained mobile robot motion planning in state lattices," *Journal of Field Robotics*, vol. 26, no. 1, pp. 308–333, Mar. 2009.

[39] M. Likhachev and D. Ferguson, "Planning long dynamically-feasible maneuvers for autonomous vehicles," *Int. J. Robotics Research*, vol. 28, no. 8, pp. 933–945, 2009.

[40] J. King and M. Likhachev, "Efficient cost computation in cost map planning for non-circular robots," in *IEEE/RSJ Int. Conf. Intelligent Robots and Systems (IROS)*, 2009, pp. 3924–3930.

[41] T. Lindeberg, "Edge detection and ridge detection with automatic scale selection," *Int. J. Computer Vision*, vol. 30, no. 2, pp. 117–156, 1998.

[42] H. Shikata, G. McLennan, E. A. Hoffman, and M. Sonka, "Segmentation of pulmonary vascular trees from thoracic 3D CT images," *Journal of Biomedical Imaging*, vol. 2009, pp. 24–34, 2009.

[43] P. J. Swaney, J. Burgner, H. B. Gilbert, and R. J. Webster, "A flexure-based steerable needle: high curvature with reduced tissue damage," *IEEE Trans. Biomedical Engineering*, vol. 60, no. 4, pp. 906–909, 2013.